SPECIAL ISSUE: Optical Gain Materials towards Enhanced Light-Matter Interactions

Epitaxial growth of metal-semiconductor van der Waals heterostructures NbS₂/MoS₂ with enhanced performance of transistors and photodetectors

Peng Zhang[1†], Ce Bian[2†], Jiafu Ye[3†], Ningyan Cheng[4], Xingguo Wang[1], Huaning Jiang[1], Yi Wei[5], Yiwei Zhang[1], Yi Du[4,6], Lihong Bao[2,7*], Weida Hu[3*] and Yongji Gong[1*]

ABSTRACT Two-dimensional (2D) heterostructures based on layered transition metal dichalcogenides (TMDs) have attracted increasing attention for the applications of the next-generation high-performance integrated electronics and optoelectronics. Although various TMD heterostructures have been successfully fabricated, epitaxial growth of such atomically thin metal-semiconductor heterostructures with a clean and sharp interface is still challenging. In addition, photodetectors based on such heterostructures have seldom been studied. Here, we report the synthesis of high-quality vertical NbS₂/MoS₂ metallic-semiconductor heterostructures. By using NbS₂ as the contact electrodes, the field-effect mobility and current on-off ratio of MoS₂ can be improved at least 6-fold and two orders of magnitude compared with the conventional Ti/Au contact, respectively. By using NbS₂ as contact, the photodetector performance of MoS₂ is much improved with higher responsivity and less response time. Such facile synthesis of atomically thin metal-semiconductor heterostructures by a simple chemical vapor deposition strategy and its effectiveness as ultrathin 2D metal contact open the door for the future application of electronics and optoelectronics.

Keywords: metal-semiconductor heterostructures, contact engineering, field-effect transistor, photodetector

INTRODUCTION

Two-dimensional (2D) materials are promising building elements for the future high-performance electronic and optoelectronic devices due to their intriguing properties, such as superconductivity, charge-density-wave state, tunable bandgap, ferromagnetic, and quantum hall effect [1–5]. The diversity of these fascinating properties based on 2D materials offers a great opportunity for constructing atomically thin heterostructures to achieve various functions and applications. Benefiting from the weak interlayer van der Waals (vdW) interaction, atomically thin 2D materials can be stacked vertically or laterally, which undoubtedly provides more possibilities to explore novel chemical and physical properties [6–10]. Recently, the vdW heterostructures play an active and crucial role in modern electronics, such as tunneling transistors, wearable electronic, and photodetectors [11–14]. Previous studies have mainly focused on the fabrication of semiconductor-semiconductor heterostructures, such as MoS₂/WS₂, WSe₂/MoSe₂ vertical heterostructures and WS₂/WS₂(1−x)Se₂x, MoS₂/WS₂ lateral heterostructure [15–17]. However, only a few metal-semiconductor heterostructures have been successfully achieved due to the uncontrollable synthesis of 2D metallic transition metal

[1] School of Materials Science and Engineering, Beihang University, Beijing 100191, China
[2] Institute of Physics & University of Chinese Academy of Sciences, Chinese Academy of Sciences, Beijing 100190, China
[3] State Key Laboratory of Infrared Physics, Shanghai Institute of Technical Physics, Chinese Academy of Sciences, Shanghai 200083, China
[4] Institute for Superconducting and Electronic Materials (ISEM), Australian Institute for Innovation Materials (AIIM), University of Wollongong, Wollongong, NSW 2522, Australia
[5] State Key Laboratory of Organic-Inorganic Composites, Beijing Key Laboratory of Electrochemical Process and Technology for Materials, Beijing University of Chemical Technology, Beijing 100029, China
[6] Beihang-UOW Joint Research Centre and School of Physics, Beihang University, Beijing 100191, China
[7] Songshan Lake Materials Laboratory, Dongguan 523803, China
[†] These authors contributed equally to this work.
[*] Corresponding authors (emails: lhbao@iphy.ac.cn (Bao L); wdhu@mail.sitp.ac.cn (Hu W); yongjigong@buaa.edu.cn (Gong Y))

dichalcogenides (TMDs) so far. The previously obtained metal-semiconductor heterostructures are usually composed of monolayer semiconducting TMDs with relatively thick metallic TMDs, lacking the advantages of ultrathin nature of 2D materials [18–20]. Although the atomically thin NbS_2/MoS_2 metal-semiconductor heterostructure has been grown by Fu *et al.* [18], its electronic and optoelectronic properties have not been systematically studied. Therefore, it is still challenging but worthwhile to fabricate atomically thin metal-semiconductor TMD heterostructures with a clean and sharp interface and explore their intriguing properties and potential applications.

Initially, it was reported that the 1T phase MoS_2, converted from 2H MoS_2 by the treatment of *n*-BuLi, can be served as contact electrodes to improve the device performance [13]. Considering the fact that damage and contaminations from the complicated process are inevitable and 1T phase MoS_2 is not stable, direct growth of 2D metallic materials as contact may be a more reliable and efficient method to improve the device performance. Up to now, chemical vapor deposition (CVD) is the most efficient approach to prepare metallic 2D materials and semiconductor-metal heterostructures. For example, VS_2 nanoflake was prepared by CVD firstly, then the nanoflake was taken as a seed to grow lateral VS_2/MoS_2 heterostructures or transferred to stack VS_2/MoS_2 heterostructures [19,20]. However, the thickness of VS_2 cannot be controlled down to atomically thin and the effect of metallic contact on optoelectronics has not been explored. Therefore, the ability to controllably grow atomically thin metal-semiconductor heterostructures with clean and sharp interface still remains challenging.

Here, we report a two-step CVD method to synthesize NbS_2/MoS_2 vertical heterostructures, where monolayer NbS_2 is epitaxially grown on the top surface of the monolayer MoS_2 and the thickness of NbS_2 can be well controlled down to monolayer. Raman and photoluminescence (PL) spectroscopy were used to confirm the formation of MoS_2 and NbS_2 and their optical coupling effect. Transmission electron microscopy (TEM) images reveal the high-quality NbS_2/MoS_2 heterostructures with a distinct interface. The fabricated MoS_2/NbS_2 heterostructure devices with NbS_2 as contact electrodes show remarkably improved device performance. The field-effect mobility and current on/off ratio of MoS_2 have been improved at least six times and two orders of magnitude compared with the conventional Ti/Au contact. In addition, by NbS_2 contact engineering, the response and recovery times of MoS_2 photodetector can be efficiently reduced at least thirty and one hundred times, respectively, while the photo-responsivity can be improved about twenty times. We believe that our work will provide a convenient avenue and new direction to design and synthesize 2D metal-semiconductor heterostructures with enhanced and synergistic device properties.

METHODS

Synthesis of atomically thin NbS_2/MoS_2 heterostructures

NbS_2/MoS_2 metal-semiconductor heterostructures were synthesized by ambient-pressure CVD in a 2-inch quartz tube heated by a Lindberg/Blue M (HTF55342C) furnace. Firstly, pristine monolayer MoS_2 was fabricated as the vdW substrate of NbS_2 on SiO_2 (300 nm)/Si. Molybdenum trioxide (MoO_3) powder and sulfur (S) powder were used as the precursors, which were placed at the center and upstream of the quartz tube, where the temperatures were set as 640 and 190°C, respectively. Before the growth, the furnace tube was purged with 500 sccm Ar for 20 min, and 80 sccm Ar was used as carrier gas during growth. The furnace was heated to 640°C in 14 min and maintained at that temperature for 3 min to allow the synthesis of MoS_2 monolayer. The furnace was naturally cooled to 600°C without changing the carrier gas. Then the top cover of the furnace was opened to allow fast cooling of the sample, with carrier gas switched to 500 sccm Ar. After the growth of MoS_2, it was transferred to another quartz tube to synthesize NbS_2/MoS_2 heterostructures immediately. Nb_2O_5 powder with NaCl and S powder (Alfa Aesar, purity 99.5%) were used as precursors, where the temperatures were set to 800 and 200°C, respectively. $MoS_2/SiO_2/Si$ was placed facing down to $Nb_2O_5/NaCl$ mixture powder. During the growth of NbS_2, 200 sccm Ar and 15 sccm H_2 were used as the carrier gases. The furnace was heated to 800°C in 17 min and maintained at that temperature for 3–5 min to allow the synthesis of NbS_2/MoS_2 layers.

Transfer of NbS_2/MoS_2 heterostructures for HAADF-STEM measurement

Poly(methyl methacrylate) (PMMA) (950 PMMA A4, Micro Chem) assisted method was used to transfer the samples for TEM measurement. The as-grown heterostructures were spin-coated with PMMA at a speed of 3000 r min^{-1} for 60 s followed by baking at 60°C for 5 min. SiO_2 layer was etched by 3% hydrofluoric acid (HF) for 10 min. After that, the lifted off PMMA/sample layer was transferred to deionized water and rinsed three times rapidly. Then, the rinsed PMMA/sample layer was

transferred onto copper grid and baked at 60°C for 5 min. Lastly, PMMA was washed off with acetone and iso-propanol.

Characterizations of NbS$_2$/MoS$_2$ heterostructures

An optical microscope (OM, Olympus CX41) was used to characterize the morphologies of NbS$_2$/MoS$_2$ hetero-structures. Jobin-Yvon LabRAM HR 800 Raman spectrometer with 532-nm laser excitation was applied to record the Raman and PL spectra and the corresponding mappings. X-ray photoelectron spectroscopy (XPS) tests were carried out *via* Thermo Scientific Escalab 250Xi. The thickness of heterostructures was characterized by an atomic force microscope (Bruker Icon). Scanning TEM (STEM) images were obtained using JEOL ARM-200CF operated at 80 kV.

Field-effect transistor (FET) device fabrication and measurement of NbS$_2$/MoS$_2$ heterostructures

Electron-beam lithography was used to define the contact regions on the heterostructures and pristine monolayer MoS$_2$ followed by electron-beam evaporation to coat a Ti/Au metal layer (5/60 nm) as contact electrodes. Device characterizations were conducted by using a Keithley 4200-SCS Parameter Analyzer in a probe station under vacuum at room temperature. The photoelectrical properties were measured in atmospheric environment, and the laser of 520 nm was illuminated on the devices using confocal microscopy.

RESULTS AND DISCUSSION

Pristine monolayer MoS$_2$ was grown first by a CVD method as reported by previous work [21]. Briefly, MoO$_3$ powder and S powder were used as the precursors, which were placed at the center and upstream of the quartz tube, respectively. For the MoS$_2$/NbS$_2$ heterostructure growth, the as-grown MoS$_2$/SiO$_2$/Si was placed face down to the mixed powder of Nb$_2$O$_5$ and NaCl at the center of the furnace [21]. The growth temperature of MoS$_2$ and NbS$_2$ was about 640 and 800°C, respectively. The growth process and the crystal structures of NbS$_2$/MoS$_2$ heterostructure are shown in Fig. 1a and Fig. S1. The morphologies of individual monolayer MoS$_2$ and NbS$_2$ examined by optical microscopy are shown in the inset of Fig. 1a, and the size of the as-prepared MoS$_2$ and NbS$_2$ is a few tens of micrometers. Fig. 1b–d show the atomic models of MoS$_2$, NbS$_2$, and the related heterostructures, where both the monolayer MoS$_2$ and NbS$_2$ are in H phase. With the growth conditions of NbS$_2$ and MoS$_2$ carefully optimized, their 2D heterostructures can be easily

achieved by this two-step growth process. The typical optical images of various as-grown NbS$_2$/MoS$_2$ hetero-structures are shown in Fig. 1e–g, where the surface of MoS$_2$ is covered by high-quality and homogeneous NbS$_2$ and sharp optical contrast can be observed between the MoS$_2$ and NbS$_2$. Based on the morphologies of hetero-structures, two possible growth modes could be proposed as follows. (1) Edge growth mode, where the enegetically active edges of bottom-layer MoS$_2$ serve as the nucleation sites for NbS$_2$, which grows from the MoS$_2$ edges and gradually covers the whole surface of MoS$_2$, as shown in Fig. 1e. (2) Central growth mode, where the nucleation sites of MoS$_2$ located at the center further assist the growth of NbS$_2$. The full coverage NbS$_2$/MoS$_2$ is shown in Fig. 1g. The relatively high density and aligned edge orientations of NbS$_2$/MoS$_2$ heterostructures indicate the high-yield and epitaxial nature of the growth. Due to the very similar local atomic bonding environment for the Nb and Mo atoms and the small lattice mismatch between NbS$_2$ and MoS$_2$, monolayer NbS$_2$ can be epitaxial grown on top of MoS$_2$ [18,22]. The morphology and height topography from AFM images are shown in Fig. S2. The thicknesses of MoS$_2$ and NbS$_2$ are about 0.78 and 0.82 nm, respectively, indicating that both the MoS$_2$ and NbS$_2$ can be tuned down to monolayer. In addition, the optical images of typical large-scale NbS$_2$/MoS$_2$ hetero-structures, with the size measured up to 100 μm, as shown in Fig. S3, indicate the size control ability of the heterostructures.

Raman and PL spectroscopy with a 532-nm laser excitation (spot size about 1 μm in diameter) were conducted to characterize the heterostructure and determine the spatial distribution of MoS$_2$ and NbS$_2$. A typical optical image of the MoS$_2$/NbS$_2$ heterostructure is shown in Fig. 2a. The apparent contrast difference in the hetero-structure indicates a clean and sharp interface between MoS$_2$ and NbS$_2$. Raman spectra of the heterostructure are shown in Fig. 2b, where the phonon vibration modes can be clearly recognized from the spectra. The Raman spectra from the MoS$_2$ area show two characteristic peaks located at about 385.1 and 404.8 cm^{-1}, which can be assigned to the in-plane E$_2$ and out-of-plane A$_1$ vibration modes, respectively (green curve in Fig. 2b) [23,24]. The frequency difference between E$_2$ and A$_1$ modes is 19.7 cm^{-1}, indicating the MoS$_2$ is single-layered. For pure NbS$_2$, the characteristic peaks of I, E$_1$, E$_2$, and A$_1$ can be found at about 147.5, 303.8, 340.9 and 379.1 cm^{-1}, respectively (purple spectrum) [25,26]. The orange spectrum in Fig. 2b represents the Raman curve of the NbS$_2$/MoS$_2$ heterostructure, where the vibration modes of MoS$_2$
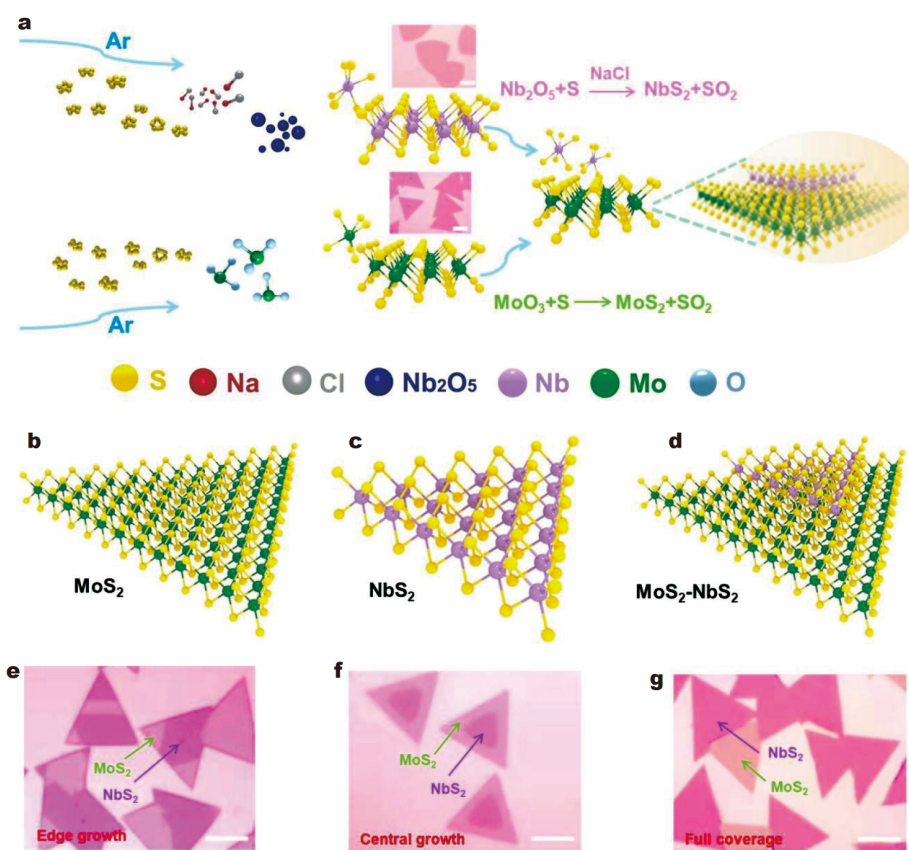
Figure 1 Synthesis and morphologies of the atomically thin NbS₂/MoS₂ vertical heterostructures. (a) Schematic of the synthesis of the NbS₂/MoS₂ heterostructures. (b–d) Structure models of pristine MoS₂, NbS₂, and NbS₂/MoS₂ heterostructure, respectively. (e–g) Optical images of the NbS₂/MoS₂ heterostructures. Two types of growth modes can be identified from the optical pictures. All the scale bars are 20 μm.

and NbS₂ can be identified. Note that the A_1 peak of NbS₂ is overlapped with the peak of E_2 mode of MoS₂, which cannot be distinguished directly. Fig. 2c shows the PL spectra of pure MoS₂ and the NbS₂/MoS₂ heterostructure. For the MoS₂ area, a very strong PL characteristic peak located at about 668 nm is observed, which is in good agreement with the reported value of monolayer MoS₂ [23,24]. However, the PL of the bottom MoS₂ is quenched by the fast charge transfer process from the NbS₂/MoS₂ heterostructure area due to their strong interlayer coupling. To further determine the chemical composition of the NbS₂/MoS₂ heterostructure, XPS was performed. As shown in Fig. 2d, the Nb^{4+} $3d_{5/2}$ and $3d_{3/2}$ core levels can be identified, whose peaks are located at ~203.1 and ~206.1 eV, respectively, in good agreement with the values from NbS₂ [27–29]. The presence of Mo^{4+} $3d_{5/2}$ and $3d_{3/2}$ peaks are marked at 229.4 and 232.5 eV, respectively. The S $2p_{3/2}$ and $2p_{1/2}$ core levels are split into four peaks located at about 160.9, 161.9, 163.1 and 164.0 eV, respectively, due to the chemical shift of S between MoS₂

and NbS₂. The peak located at 160.9 and 161.9 eV are attributed to Nb–S $2p_{3/2}$ and $2p_{1/2}$, respectively, while the binding energy of 163.1 and 164.0 eV should be assigned to Mo–S $2p_{3/2}$ and $2p_{1/2}$ core levels [30,31]. All these peaks match well with the values of the MoS₂ and NbS₂ systems. The original XPS spectrum is shown in Fig. S4. It is worth noting that the atomic ratio of Mo–S and Nb–S from the XPS spectra is about 1:2, which further confirms the stoichiometry of MoS₂ and NbS₂.

High-angle annular dark-field STEM (HAADF-STEM) was performed to further investigate the crystal quality and detailed atomic structures of the NbS₂/MoS₂ heterostructure. Fig. 3a is the low-magnification atomic-resolution HAADF-STEM image of the heterostructure, where monolayer NbS₂ (upper layer) and MoS₂ (bottom layer) can be distinguished directly. HAADF-STEM image of monolayer MoS₂ and the NbS₂/MoS₂ heterostructure are shown in Fig. 3b and c, respectively, where the samples are of high crystallinity. The atomically sharp interface between NbS₂ and MoS₂ is highlighted by the
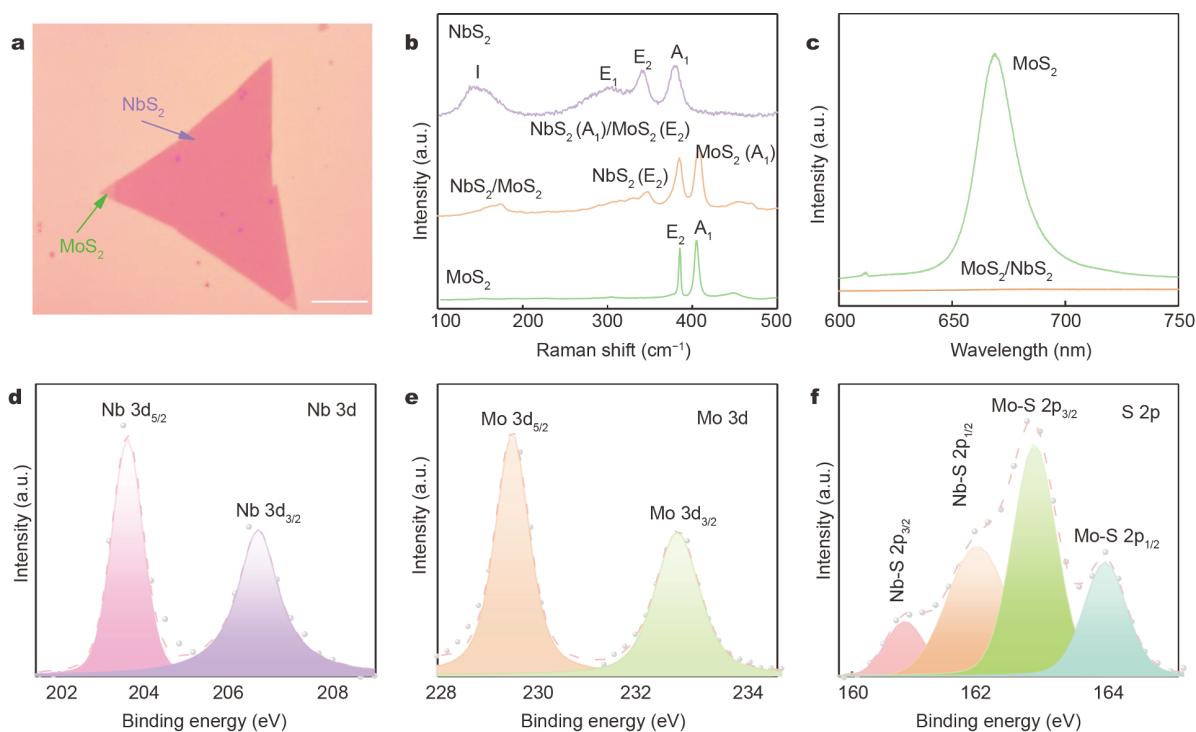
Figure 2 Raman, PL and XPS characterizations of the NbS_2/MoS_2 heterostructures. (a) Optical image of the typical NbS_2/MoS_2 heterostructure, where high quality atomically thin NbS_2 epitaxial grows on top of MoS_2 except the corner. The scale bar is 20 μm. (b) Raman spectra of MoS_2, NbS_2 and NbS_2/MoS_2 heterostructures. (c) PL spectra of NbS_2 and NbS_2/MoS_2 heterostructures. (d–f) XPS curves of Nb 3d, Mo 3d and S 2p core levels from the heterostructures.

olive dashed line in Fig. 3c. The bilayer heterostructure region of NbS_2/MoS_2 shows clear Moiré patterns from Fig. 3d, which can be assigned to the overlapping lattice of NbS_2 and MoS_2. The periodic cell of Moiré pattern highlighted by the red dashed rhombus is about 6.5 nm, consistent with previous reports [18]. The corresponding fast Fourier transformation (FFT) images of bilayer NbS_2/MoS_2 heterostructure area are presented in Fig. 3e and f, where two sets of hexagonally arranged diffraction spots can be distinguished as magnified and labeled in Fig. 3f. The detailed FFT image of monolayer MoS_2 is shown in Fig. S5. The lattice constants of NbS_2 and MoS_2 are 0.34 and 0.32 nm, respectively, measured from the diffraction spots. In addition, the identical orientations of the two sets of diffraction spots show that there is no twist angle between the NbS_2 and MoS_2. Fig. 3g and h show the top and side views of the simulation atomic structure model of the NbS_2/MoS_2 heterostructure with Moiré patterns, consistent with the experimental results shown in Fig. 3d. Considering the clean surface and sharp boundary, distinct Raman vibration modes, strong PL characteristic peak and unbroken atomic structure of MoS_2, it can be concluded that the MoS_2 will be well kept after growth of

NbS_2.

Given the excellent electrical conductivity of metallic NbS_2, it can be served as the efficient contact material to optimize the device performance in 2D electronics. MoS_2 field-effect transistors (FETs) with NbS_2 as the contact electrodes were fabricated based on our CVD-grown heterostructures, and the optical images of such devices are shown in Fig. S6a–c. Fig. 4a–c show the schematic diagram of MoS_2 devices with different contacts and their corresponding output characteristics are presented in Fig. 4d–f and Fig. S6d–f. The on-state current is 1.5 μA μm^{-1} at bias voltage V_{ds}=1.0 V and back-gate voltage V_{bg} =60 V for two-terminal NbS_2 contacted MoS_2 FET (Fig. 4f), which is about ten times more than that with Ti/ Au contact (Fig. 4d) and is about five times of the on-state current from one-terminal NbS_2 contacted MoS_2 FET (Fig. 4e). The significant improvement of on-state current can be attributed to the metallic NbS_2 contact, and the electrical conductivity of NbS_2 is shown in Fig. S6g and h. The interface damage, structural distortion, and Fermi level pinning effect due to Ti/Au deposition can be effectively avoided by the presence of epitaxially grown NbS_2 layer as vdW contact. Thus, the
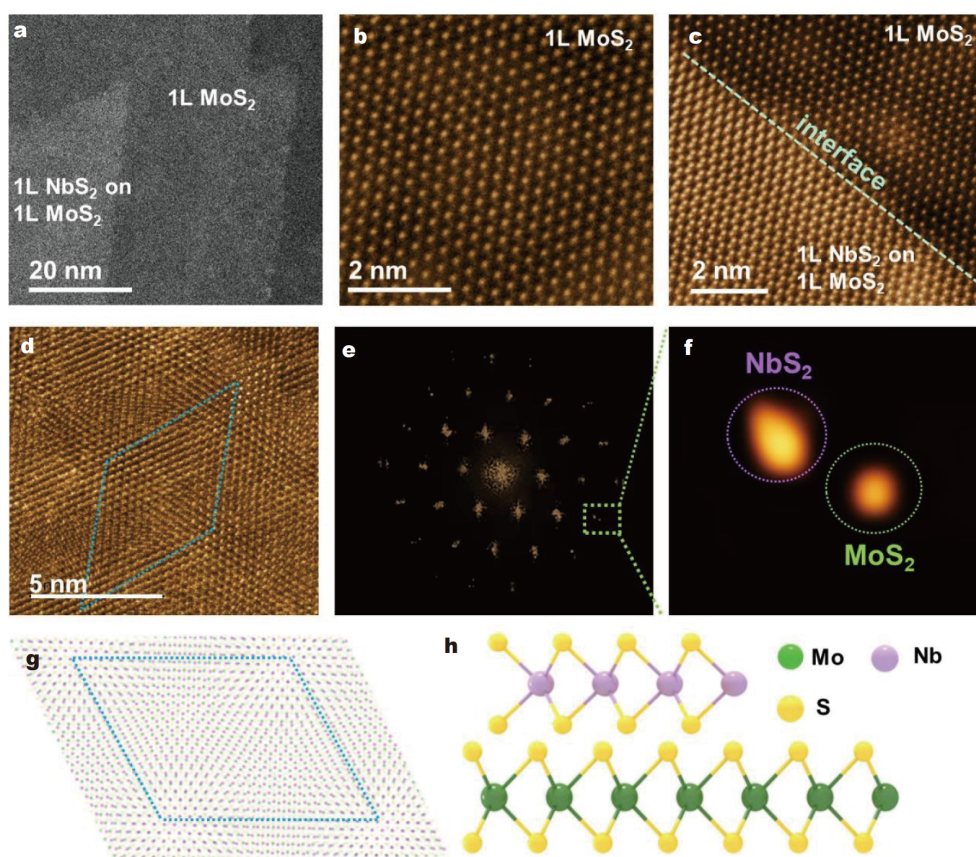
Figure 3 Atomic structure of the NbS_2/MoS_2 heterostructure. (a) Low magnification of HAADF-STEM image of the vertically stacked heterostructure, where the region of MoS_2 and interface of NbS_2/MoS_2 can be distinguished clearly. 1L stands for one layer. (b) HAADF-STEM image of monolayer MoS_2. Scale bar, 2 nm. (c) HAADF-STEM image of the NbS_2/MoS_2 heterostructure, where atomically sharp interface was highlighted by the olive dashed lines. Scale bar, 2 nm. (d) HAADF image taken from the region of heterostructure, indicating the periodic Moiré pattern. Scale bar, 5 nm. (e, f) FFT patterns collected from the heterostructure region and the magnified view of reciprocal lattices of NbS_2 and MoS_2, marked by purple and green circles, respectively. (g, h) Atomic structures of the NbS_2/MoS_2 heterostructure from top view and side view.

Schottky barrier and contact resistance should be much smaller for MoS_2 FET with NbS_2 contact than that with Ti/Au contact [19,32,33]. The transport behavior of NbS_2 is shown in Fig. S6g and h, where a linear I_{ds}-V_{ds} curve can be obtained, indicating the Ohmic contact between NbS_2 and electrodes. Note that the current is about 0.1 mA at V_{ds}=0.1 V, showing the metallic nature and the excellent electrical conductivity. Fig. 4g compares the output characteristics of the MoS_2 devices with NbS_2 and Ti/Au contacts under V_{bg}=60 V. The corresponding transfer curves are shown in Fig. 4h, showing a typical n-type behavior of the MoS_2 channel. The current on-off ratio is 1.8×10^7 for the two-terminal NbS_2 contacted MoS_2 FET, about two orders of magnitude larger than that for the Ti/Au contact ($\sim 8.4 \times 10^5$). The carrier mobility can be derived from the standard formula of $\mu = dI_{ds}/dV_{bg} \cdot (L/WC_iV_{ds})$, where W and L are the width and length of

the channel, C_i is the capacitance with 11.5 nF cm^{-2}, V_{ds} = 2 V. The calculated mobility (μ_{FE}) of MoS_2 FET with two-terminal NbS_2 contact reaches 15 cm^2 V^{-1} s^{-1} (W=2.1 μm, L=2.5 μm), which is about six times that with the Ti/Au contact (μ_{FE}=2.5 cm^2 V^{-1} s^{-1},W=7 μm, L=5 μm). These three devices show similar threshold voltages (~ -40 V) and subthreshold swings (3.2 V dec^{-1}), indicating that the doping level and the density of gap states in the MoS_2 channel are nearly the same [19]. Notably, each kind of contact is tested for at least three devices and all of them show consistent mobilities and on-off ratios. The results demonstrate that the device performance can be greatly improved by the NbS_2 contact. The parameters of the channel widths, lengths, mobility and on-off ratio are summarized in Table S1 (Supplementary information). It should be noted that the MoS_2 is well kept and will not be doped by Nb atoms after the growth of NbS_2, which is
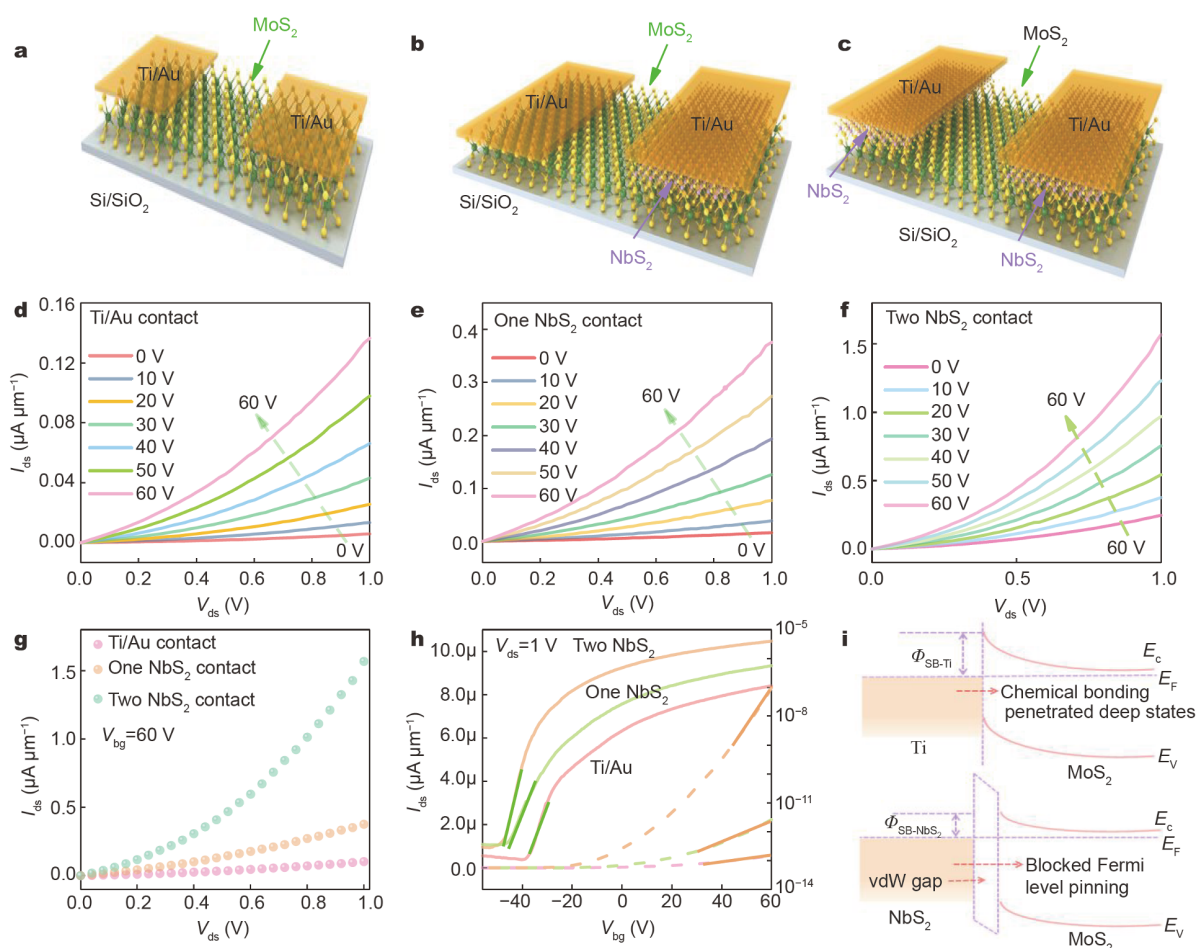
Figure 4 MoS_2 FETs with Ti/Au and NbS_2 as contacts. (a–c) The schematic models of MoS_2 FETs with Ti/Au contact, one NbS_2 contact and two NbS_2 contacts, respectively. (d–f) Output characteristics of the MoS_2 FETs with different contacts. (g) The comparison of output characteristics of MoS_2 with different contacts at V_{bg}=60 V. (h) Transfer curves of the MoS_2 FETs with different contacts. (i) Band diagrams of the Ti/MoS_2 and NbS_2/MoS_2 interfaces, respectively.

demonstrated by the preserved strong PL intensity, similar carrier concentration and electrical characteristic [20,22]. Therefore, all the electrical changes come from the contact engineering. The detailed calculation of the carrier density and discussion are shown in Fig. S6. In addition, the performance of the NbS_2-contacted MoS_2 device is stable and nearly unchanged after exposure in air for one week (Fig. S7).

Though it is difficult to extract the contact resistance of $R_{c\text{-}NbS_2}$ directly from transfer curves, $R_{c\text{-}NbS_2}$ can be estimated and compared with $R_{c\text{-}Ti}$ from the output curves [20]. $R_{c\text{-}NbS_2}$ and $R_{c\text{-}Ti}$ can be acquired by the following fomula:

$$2R_{c\text{-}NbS_2} = R_{on\text{-}NbS_2} - R_{ch\text{-}NbS_2},$$
$$2R_{c\text{-}Ti} = R_{on\text{-}Ti} - R_{ch\text{-}Ti}, \tag{1}$$

where $R_{ch\text{-}Ti}$ and $R_{ch\text{-}NbS_2}$ are the channel resistance and the $R_{on\text{-}Ti}$ and $R_{on\text{-}NbS_2}$ are the total resistance of Ti/Au and two NbS_2 contacted MoS_2 FET, respectively. Note that

$$R_{ch\text{-}NbS_2} = L \cdot \frac{\rho_{MoS_2}}{\Delta h \cdot W} = 1.5\rho_{MoS_2} > R_{ch\text{-}Ti}$$
$$= L \cdot \frac{\rho_{MoS_2}}{\Delta h \cdot W} = 0.9\rho_{MoS_2}, \tag{2}$$

where Δh is the thickness of monolayer of MoS_2. Therefore, it can be obtained by

$$\frac{R_{c\text{-}NbS_2}}{R_{c\text{-}Ti}} < \frac{2R_{c\text{-}NbS_2} + R_{ch\text{-}NbS_2}}{2R_{c\text{-}Ti} + R_{ch\text{-}Ti}} = \frac{I_{on\text{-}Ti}}{I_{on\text{-}NbS_2}} \approx \frac{1}{10}, \tag{3}$$

where $I_{on\text{-}Ti}$ and $I_{on\text{-}NbS_2}$ are the on-state current of Ti/Au and two NbS_2 contacted MoS_2 FET, respectively. The contact resistance $R_{c\text{-}NbS_2}$ is less than 1/10 that of Ti/Au contact. Besides, according to the formula [34]

$$R_{\text{on}} = L/\mu_{\text{FE}}C_iW(V_{\text{GS}} - V_{\text{TH}}), \tag{4}$$

where the μ_{FE}, C_i, V_{GS} and V_{TH} are the mobility, capacitance, gate and threshold voltage, respectively. The ratio of $R_{\text{c-NbS}_2}/R_{\text{c-Ti}}$ also can be acquired by

$$R_{\text{c-NbS}_2}/R_{\text{c-Ti}} < R_{\text{on-NbS}_2}/R_{\text{on-Ti}} \approx 1/7. \tag{5}$$

The contact resistance of $R_{\text{c-NbS}_2}$ is less than 1/7 that of Ti/Au contact, consistent with the results obtained from the on-state current. Therefore, the improved on-state current, on-off ratio, and mobility can be attributed to the decreased contact resistance as well as the lowered Schottky barriers (Φ_{SB}) height [19,31,32]. It is reported that the Φ_{SB} can decrease from 163 meV (Ni/Au contact) to 30 meV (VS_2 contact), which can be attributed to the absence of Fermi level pinning effects between the VS_2 and MoS_2 interface [19,35–38]. Considering the similar work function of VS_2 and NbS_2 [20,38], and the decreased contact resistance, the Φ_{SB} in the NbS_2/MoS_2 interface should also be smaller than that for Ti/Au contact. Fig. 4i shows the schematics of the band alignments of the Ti/MoS_2 and NbS_2/MoS_2 interface, respectively. For Ti/Au contact, the surface of MoS_2 will be damaged by the metal contact directly, which was verified by Liu et al. [39]. In addition, chemical bonding will be formed in the Ti/MoS_2 interface and the deep energy level states may be penetrated close to the conduction band due to the Fermi level pinning effects [19,20,39]. However, the Fermi level pinning effects and surface damage of MoS_2 will be blocked by the protection of NbS_2, where the height of Φ_{SB} as well as the contact resistance will be reduced.

To further evaluate the effect of the NbS_2 contacts, the photodetector was fabricated based on the NbS_2/MoS_2 vdW heterojunctions. The schematic diagram of the MoS_2 photodetector is shown in Fig. 5a and b, where the wavelength of the incident light is 520 nm. Fig. 5c shows the photocurrent switching behavior of MoS_2 transistor with two NbS_2 contacts under different illumination power densities at $V_{\text{ds}}=1$ V, where the device exhibits excellent sensitivity, repeatability, and stability. It is worth mentioning that a high laser power density would have a thermal effect on the MoS_2 transistor. When the laser is turned off, most photocurrents would decrease quickly, and residual thermal-induced current can decrease tardily by heat dissipation process. Fig. 5d–f show the photocurrent switching on-off curves and response time of MoS_2 detector with Ti/Au contact. It can be seen that there is no steady photocurrent terrace, indicating that there are many defects in the lattice of MoS_2 [40–42]. According to the 10% and 90% photocurrent values of a single on/off cycle, shown in Fig. 5e and f, the response

and recovery times of the devices are about 1.0 and 7.1 s, respectively. The photon-generated carrier will be recombined at defective sites during the conduction of photocurrent, decreasing the sensitivity of MoS_2 greatly. However, it is surprising to find that the sensitivity and stability of photocurrent of MoS_2 can be regulated and improved significantly by NbS_2 contacts. Fig. 5g records the photocurrent switching behavior of the MoS_2 device with NbS_2 contact. The response and recovery times are about 30 and 70 ms, respectively, which is thirty and one hundred times faster than that for the Ti/Au contact device. Considering the similar defect distribution in the channel of the device, the improved performance can be attributed to the decreased contact resistance and lowered Schottky barrier height. The decreased contact barrier may provide a more unblocked way to collect photon-generated carriers, which will decrease the rate of carrier recombination and accelerate the generation of photo-excited charge carriers. In addition, no extra interface and crystal defects were introduced due to the protection of NbS_2 interlayer, the carrier scattering can be greatly reduced in the interface [39,43]. Therefore, the response time in the NbS_2-contacted MoS_2 is faster than that for the Ti/Au-contacted counterpart. The detailed mechanisms and microscopic picture as well as the corresponding discussion can be seen in Fig. S8. The photo-responsivity was obtained to further evaluate the promotion of the NbS_2 contacted photodetector. According to the equation $R=(I_{\text{photo}}-I_{\text{dark}})/P$, where the I_{photo} and I_{dark} are the photocurrent and dark current, respectively, and P is 30 nW, representing the effective incident power on the device channel [44]. The photo-responsivity can be improved from 64.9 mA W^{-1} for the Ti/Au-contacted MoS_2 device to 1.27 A W^{-1} for the NbS_2-contacted counterpart with the laser power density of 42.5 mW mm^{-2}. The photo-responsivity curves with different power densities are shown in Fig. S9. In addition, the photo-responsivity is much higher than that for the MoS_2/glassy-graphene system (12.3 mA W^{-1}), pure SnS_2 (9 mA W^{-1}) and $MoSe_2$ (0.26 mA W^{-1}) photodetector, and comparable to the dye-sensitized MoS_2 (1.17 A W^{-1}), and pure $GaSe$ (2.8 A W^{-1}) photodetector (see Table 1 for details) [37–50]. The above results demonstrate the excellent improvements of device performance by the NbS_2 contact, providing a competitive candidate in the field of the optoelectronic system.

CONCLUSIONS

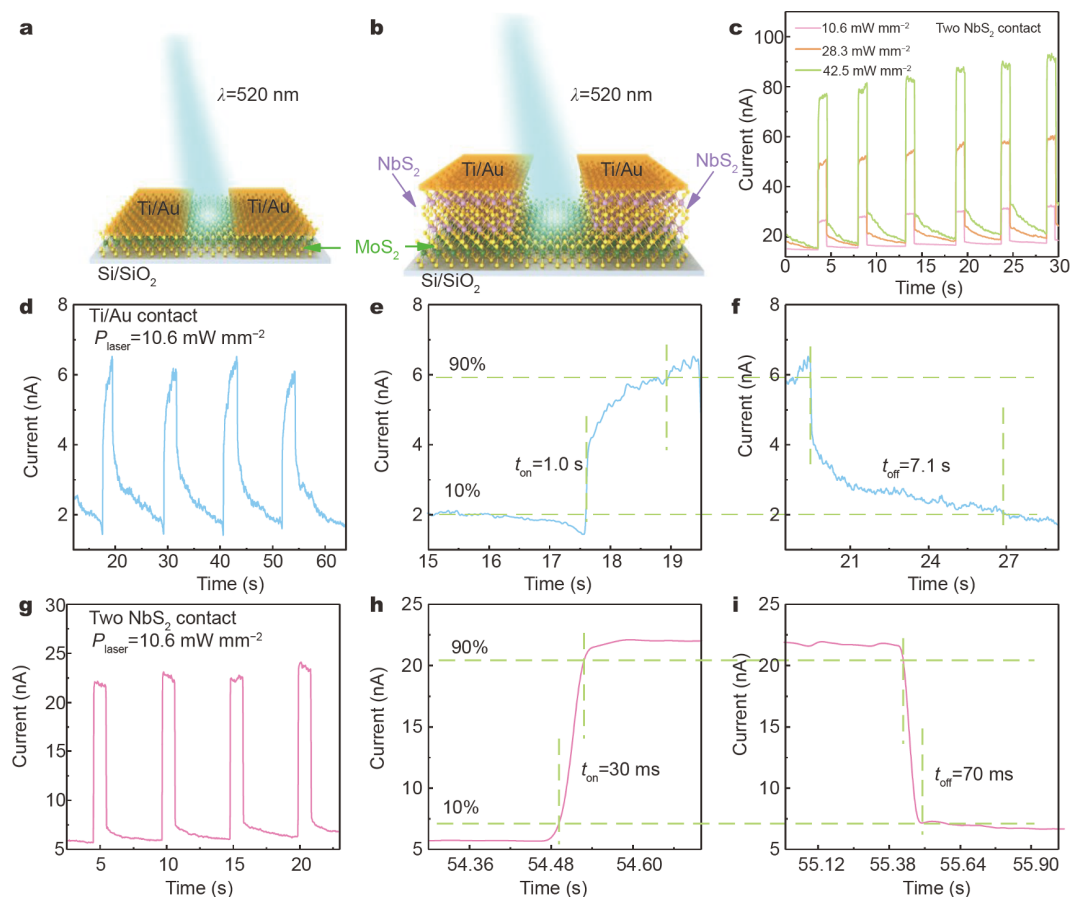In conclusion, we have successfully epitaxially grown high-quality atomically thin metal-semiconductor $NbS_2/$

Figure 5 MoS$_2$ photodetectors with Ti/Au and NbS$_2$ as contacts. (a, b) Structural schematics of the Ti/Au and NbS$_2$ (two terminals)-contacted MoS$_2$ photodetectors with 532-nm laser illumination. (c) Time-resolved photocurrents of the NbS$_2$-contacted MoS$_2$ photodetectors with different power densities. (d–f) The photocurrent switching on-off curves and response time of MoS$_2$ detector with Ti/Au contact. (g–i) The photocurrent switching on-off curves and response time of the MoS$_2$ detector with NbS$_2$ contact.

Table 1 Performance comparison of the MoS$_2$ device with NbS$_2$ contact and other 2D materials produced by mechanical exfoliation or CVD methods (1L stands for one layer)

Device	Fabrication method	Mobility (cm^2 V^{-1} s^{-1})	$I_{on/off}$ ratio	μ_{FE} improved	Photodetector rise/decay time	Spectral Res. (mA W^{-1})	Refs.
VS$_2$-MoS$_2$	CVD	35	10^6	Six-time	–	–	[19]
VS$_2$-MoS$_2$	CVD	7.8	10^6	Four time	–	–	[20]
NbS$_2$-WS$_2$	CVD	0.14	10^5	Equal	–	–	[25]
Gra-MoS$_2$	CVD	8.6	10^9	Five-time	–	–	[32]
NbTe$_2$-WSe$_2$	CVD	12.1	10^6	Twice	–	–	[33]
Ag-MoS$_2$	CVD	–	–	–	0.3 s/1.6 s	7.94×10^6	[40]
1L MoS$_2$	CVD	0.23	10^5	–	55 ms/1.0 s	7.8×10^5	[41]
1L MoS$_2$	Exfoliation	0.11	10^3	–	50 ms/50 ms	7.5	[42]
1L MoS$_2$	Exfoliation	4.0	–	–	0.6 s/9.0 s	8.8×10^5	[44]
1L MoSe$_2$	CVD	15	10^5	–	25 ms/–	2.6×10^{-1}	[45]
FL GaS	Exfoliation	–	10^4	–	30 ms/30 ms	9.5×10^2	[46]
FL GaSe	CVD	–	10^2	–	–	6×10^2	[47]
FL GaSe	CVD	–	10^4	–	120 ms/150 ms	2.6×10	[48]
NbS$_2$/MoS$_2$	CVD	15	10^7	Six-time	30 ms/70 ms	1.27×10^3	This work

MoS_2 heterostructures with a clean and sharp interface by a simple two-step CVD method. By engineering the contact using atomically thin NbS_2, the mobility of MoS_2 was improved from 2.5 to 15 cm^2 V^{-1} s^{-1}, at least six times that for the Ti/Au contact and the current on-off ratio was improved about two orders of magnitude. In addition, we demonstrate that the response time of the photodetector based on MoS_2 can be efficiently reduced while the photo-responsivity can be distinctly improved by NbS_2 contact engineering. We believe that our convenient CVD synthesis of metal-semiconductor heterostructures combining with contact engineering strategy will be a competitive candidate for the applications of 2D metallic TMDs in integrated electronics.

1   Gong Y, Yuan H, Wu CL, et al. Spatially controlled doping of two-dimensional SnS_2 through intercalation for electronics. Nat Nanotech, 2018, 13: 294–299

2   Wang C, He Q, Halim U, et al. Monolayer atomic crystal molecular superlattices. Nature, 2018, 555: 231–236

3   Wang Y, Xiao J, Zhu H, et al. Structural phase transition in monolayer $MoTe_2$ riven by electrostatic doping. Nature, 2017, 550: 487–491

4   Wang Z, Gibertini M, Dumcenco D, et al. Determining the phase diagram of atomically thin layered antiferromagnet $CrCl_3$. Nat Nanotechnol, 2019, 14: 1116–1122

5   Liao M, Wu ZW, Du L, et al. Twist angle-dependent conductivities across MoS_2/graphene heterojunctions. Nat Commun, 2018, 9: 4068

6   Zhou X, Hu X, Zhou S, et al. Tunneling diode based on WSe_2/SnS_2 heterostructure incorporating high detectivity and responsivity. Adv Mater, 2018, 30: 1703286

7   Xiao Y, Zhang T, Zhou M, et al. Disassembly of 2D vertical heterostructures. Adv Mater, 2019, 31: 1805976

8   Luo Y, Li X, Cai X, et al. Two-dimensional MoS_2 confined $Co(OH)_2$ electrocatalysts for hydrogen evolution in alkaline electrolytes. ACS Nano, 2018, 12: 4565–4573

9   Zhang D, Du J, Hong YL, et al. A double support layer for facile clean transfer of two-dimensional materials for high-performance electronic and optoelectronic devices. ACS Nano, 2019, 13: 5513–5522

10 Liu L, Wu J, Wu L, et al. Phase-selective synthesis of 1T′ MoS_2 monolayers and heterophase bilayers. Nat Mater, 2018, 17: 1108–1114

11 Son SB, Kim Y, Kim AR, et al. Ultraviolet wavelength-dependent optoelectronic properties in two-dimensional $NbSe_2$-WSe_2 van der Waals heterojunction-based field-effect transistors. ACS Appl Mater Interfaces, 2017, 9: 41537–41545

12 Yang T, Zheng B, Wang Z, et al. Van der Waals epitaxial growth and optoelectronics of large-scale WSe_2/SnS_2 vertical bilayer p-n junctions. Nat Commun, 2017, 8: 1906

13 Lee H, Bak S, An SJ, et al. Highly efficient thin-film transistor via cross-linking of 1T edge functional 2H molybdenum disulfides.

14 Shin HG, Yoon HS, Kim JS, et al. Vertical and in-plane current devices using NbS_2/n-MoS_2 van der Waals Schottky junction and graphene contact. Nano Lett, 2018, 18: 1937–1945

15 Gong Y, Lin J, Wang X, et al. Vertical and in-plane heterostructures from WS_2/MoS_2 monolayers. Nat Mater, 2014, 13: 1135–1142

16 Hsu WT, Lu LS, Wu PH, et al. Negative circular polarization emissions from WSe_2/$MoSe_2$ commensurate heterobilayers. Nat Commun, 2018, 9: 1356

17 Xue Y, Zhang Y, Liu Y, et al. Scalable production of a few-layer MoS_2/WS_2 vertical heterojunction array and its application for photodetectors. ACS Nano, 2016, 10: 573–580

18 Fu Q, Wang X, Zhou J, et al. One-step synthesis of metal/semiconductor heterostructure NbS_2/MoS_2. Chem Mater, 2018, 30: 4001–4007

19 Leong WS, Ji Q, Mao N, et al. Synthetic lateral metal-semiconductor heterostructures of transition metal disulfides. J Am Chem Soc, 2018, 140: 12354–12358

20 Ji Q, Li C, Wang J, et al. Metallic vanadium disulfide nanosheets as a platform material for multifunctional electrode applications. Nano Lett, 2017, 17: 4908–4916

21 Zhou J, Lin J, Huang X, et al. A library of atomically thin metal chalcogenides. Nature, 2018, 556: 355–359

22 Suh J, Park TE, Lin DY, et al. Doping against the native propensity of MoS_2: Degenerate hole doping by cation substitution. Nano Lett, 2014, 14: 6976–6982

23 Zhang J, Wu J, Guo H, et al. Unveiling active sites for the hydrogen evolution reaction on monolayer MoS_2. Adv Mater, 2017, 29: 1701955

24 Jeong H, Oh HM, Gokarna A, et al. Integrated freestanding two-dimensional transition metal dichalcogenides. Adv Mater, 2017, 29: 1700308

25 Zhang Y, Yin L, Chu J, et al. Edge-epitaxial growth of 2D NbS_2-WS_2 lateral metal-semiconductor heterostructures. Adv Mater, 2018, 30: 1803665

26 Wang X, Lin J, Zhu Y, et al. Chemical vapor deposition of trigonal prismatic NbS_2 monolayers and 3R-polytype few-layers. Nanoscale, 2017, 9: 16607–16611

27 Han JH, Kim HK, Baek B, et al. Activation of the basal plane in two dimensional transition metal chalcogenide nanostructures. J Am Chem Soc, 2018, 140: 13663–13671

28 Li Z, Yang W, Losovyj Y, et al. Large-size niobium disulfide nanoflakes down to bilayers grown by sulfurization. Nano Res, 2018, 11: 5978–5988

29 Jouve G, Séverac C, Cantacuzène S. XPS study of NbN and (NbTi)N superconducting coatings. Thin Solid Films, 1996, 287: 146–153

30 Gong Y, Liu Z, Lupini AR, et al. Band gap engineering and layer-by-layer mapping of selenium-doped molybdenum disulfide. Nano Lett, 2014, 14: 442–449

31 Cui X, Kong Z, Gao E, et al. Rolling up transition metal dichalcogenide nanoscrolls via one drop of ethanol. Nat Commun, 2018, 9: 1301

32 Hong W, Shim GW, Yang SY, et al. Improved electrical contact properties of MoS_2-graphene lateral heterostructure. Adv Funct Mater, 2018, 29: 1807550

33 Wu R, Tao Q, Dang W, et al. Van der Waals epitaxial growth of atomically thin 2D metals on dangling-bond-free WSe_2 and WS_2. Adv Funct Mater, 2019, 29: 1806611

34 Li M, Lin CY, Yang SH, *et al.* High mobilities in layered InSe transistors with indium-encapsulation-induced surface charge doping. Adv Mater, 2018, 30: 1803690

35 Das S, Chen HY, Penumatcha AV, *et al.* High performance multilayer MoS₂ transistors with scandium contacts. Nano Lett, 2013, 13: 100–105

36 Abraham M, Mohney SE. Annealed Ag contacts to MoS₂ field-effect transistors. J Appl Phys, 2017, 122: 115306

37 Maurel C, Ajustron F, Péchou R, *et al.* Electrical behavior of the Au/MoS₂ interface studied by light emission induced by scanning tunneling microscopy. Surf Sci, 2006, 600: 442–447

38 Liu Y, Stradins P, Wei SH. Van der Waals metal-semiconductor junction: Weak Fermi level pinning enables effective tuning of Schottky barrier. Sci Adv, 2016, 2: e1600069

39 Liu Y, Guo J, Zhu E, *et al.* Approaching the Schottky-Mott limit in van der Waals metal-semiconductor junctions. Nature, 2018, 557: 696–700

40 Sun B, Wang Z, Liu Z, *et al.* Tailoring of silver nanocubes with optimized localized surface plasmon in a gap mode for a flexible MoS₂ photodetector. Adv Funct Mater, 2019, 29: 1900541

41 Zhang W, Huang JK, Chen CH, *et al.* High-gain phototransistors based on a CVD MoS₂ monolayer. Adv Mater, 2013, 25: 3456–3461

42 Yin Z, Li H, Li H, *et al.* Single-layer MoS₂ phototransistors. ACS Nano, 2012, 6: 74–80

43 Wang Y, Kim JC, Wu RJ, *et al.* Van der Waals contacts between three-dimensional metals and two-dimensional semiconductors. Nature, 2019, 568: 70–74

44 Lopez-Sanchez O, Lembke D, Kayci M, *et al.* Ultrasensitive photodetectors based on monolayer MoS₂. Nat Nanotech, 2013, 8: 497–501

45 Chang YH, Zhang W, Zhu Y, *et al.* Monolayer MoSe₂ grown by chemical vapor deposition for fast photodetection. ACS Nano, 2014, 8: 8582–8590

46 Hu PA, Wang L, Yoon M, *et al.* Highly responsive ultrathin GaS nanosheet photodetectors on rigid and flexible substrates. Nano Lett, 2013, 13: 1649–1654

47 Zhou Y, Nie Y, Liu Y, *et al.* Epitaxy and photoresponse of two-dimensional GaSe crystals on flexible transparent mica sheets. ACS Nano, 2014, 8: 1485–1490

48 Zeng W, Li J, Feng L, *et al.* Synthesis of large-area atomically thin BiOI crystals with highly sensitive and controllable photodetection. Adv Funct Mater, 2019, 29: 1900129

49 Zou Z, Li D, Liang J, *et al.* Epitaxial synthesis of ultrathin β-In₂Se₃/MoS₂ heterostructures with high visible/near-infrared photoresponse. Nanoscale, 2020, 12: 6480–6488

50 Liu H, Li D, Ma C, *et al.* Van der Waals epitaxial growth of vertically stacked Sb₂Te₃/MoS₂ p-n heterojunctions for high performance optoelectronics. Nano Energy, 2019, 59: 66–74

Author contributions Gong Y and Zhang P conceived and designed the experiments. Zhang P synthesized the heterojunction; Bian C made the devices and carried out the measurement; Ye J carried out the photodetector measurement; Cheng N carried out the HAADF-STEM experiments. All the authors participated in discussions and approved the manuscript.

Conflict of interest The authors declare that they have no conflict of interest.

Supplementary information Experimental details and supporting data, including the growth process, AFM, optical images, XPS, HAADF-STEM images, electrical properties are available in the online version of the paper.

Peng Zhang received his BS degree (2013) from the Department of Electronic Engineering, Nantong University, Jiangsu, and PhD degree (2018) from the Department of Electronic Engineering, East China Normal University, Shanghai. He is currently working as a postdoctoral fellow in the Department of Materials Science and Engineering, Beihang University, Beijing. His research interests focus on the controlled synthesis of novel low-dimension materials, and the application research of functional devices.

Ce Bian received his BSc degree from Shandong University. He is currently a PhD student at the Institute of Physics, Chinese Academy of Sciences. His research interests involve chemical vapor deposition and device applications of two-dimensional materials and heterostructures.

Jiafu Ye received his BS degree in materials science and engineering from Central South University, Changsha, China, in 2017. He is currently working towards his PhD degree in condensed matter physics at Shanghai Institute of Technical Physics, Chinese Academy of Sciences, under the supervision of Prof. Weida Hu. His current research interests focus on the synthesis and characterizations of novel low-dimensional materials, and their potential applications in electronic and photoelectronic devices.

Lihong Bao received his PhD degree from the Institute of Physics, Chinese Academy of Sciences. Now, he is an associate professor at the Institute of Physics, Chinese Academy of Sciences. His research interests focus on the construction and electronic transport properties of low-dimensional electronic devices.

Weida Hu received his PhD degree in microelectronics and solid-state electronics from Shanghai Institute of Technology Physics, Chinese Academy of Sciences, in 2007. He is currently a full professor in Shanghai Institute of Technology Physics, Chinese Academy of Sciences. His current research interests focus on the fabrication and characterizations of infrared photoelectronic devices.

Yongji Gong received his BS degree (2011) in chemistry from Peking University and PhD degree (2015) in chemistry from Rice University. Then, he worked as postdoctoral fellow in the Department of Materials Science and Engineering in Stanford University (2016–2017). From 2017, he has been a professor in the Department of Materials Science and Engineering, Beihang University. His scientific interest focuses on the controllable synthesis and propertiy tuning of 2D materials for electronics and energy storage and conversion.

外延生长范德华金属-半导体NbS$_2$/MoS$_2$异质结用于增强晶体管和光电探测器性能

张鹏[1†]，边策[2†]，叶家富[3†]，程宁燕[4]，王兴国[1]，江华宁[1]，魏怡[5]，张亦玮[1]，杜轶[4,6]，鲍丽宏[2,7*]，胡伟达[3*]，宫勇吉[1*]

摘要 基于过渡金属硫族化合物的二维材料异质结，由于其在下一代高性能集成光电子器件中的潜在应用而备受关注．虽然目前异质结制备很广泛，但是外延生长具有干净锐利界面的原子级别厚度金属-半导体异质结仍然备受挑战．另外，基于金属-半导体异质结的光电性能还鲜有研究．这里，我们报道了高质量垂直金属-半导体异质结的合成，其中金属性质的单层NbS$_2$外延生长于单层MoS$_2$表层．使用NbS$_2$作为电极接触的MoS$_2$晶体管，其迁移率和电流开关比相对于Ti/Au接触的MoS$_2$晶体管分别提升了6倍和2个数量级．另外，基于NbS$_2$作为电极接触的MoS$_2$光电探测器，其响应时间和光响应可以分别提升至少30倍和20倍．本工作通过简单的化学气相沉积(CVD)方法制备的原子级别厚度的金属-半导体异质结和二维金属材料在接触方面的作用为其在光电子器件中的应用奠定了基础．